Chemical Science

Accepted Manuscript

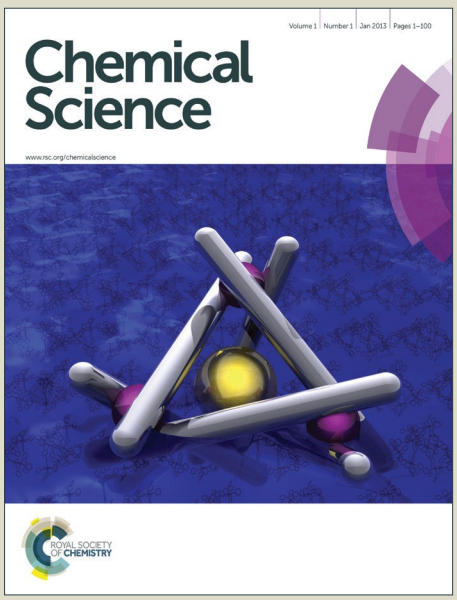

ROYAL SOCIETY OF CHEMISTRY

www.rsc.org/chemicalscience

Journal Name

ARTICLE

The Flat-on Ambipolar Triphenylamine/C_{60} Nano-Stacks Formed from the Self-Organization of a Pyramid-Sphere Shape Amphiphile

Received 00th January 20xx,
Accepted 00th January 20xx

DOI: 10.1039/x0xx00000x

www.rsc.org/

Wei-Wei Liang, [a‡] Chi-Feng Huang, [a‡] Kuan-Yi Wu, [a] San-Lien Wu,[a] Shu-Ting Chang, [a] Yen-Ju Cheng, [a] and Chien-Lung Wang [a]*

A giant shape amphiphile, which is constructed with an amorphous nano-pyramid (triphenylamine, TPA) and a crystalline nano-sphere (C_{60}), was synthesized. Structural characterizations indicate that this pyramid-sphere shape amphiphile (**TPA-C_{60}**) forms a solvent-induced ordered phase, in which the two constituent units self-assemble into alternative stacks of two-dimensional (2D) TPA and C_{60} nano-sheets. Due to the complexity of the molecular structure, and the amorphous nature of the nano-pyramid, the phase formation was driven by the intermolecular C_{60}- C_{60} interaction, and the ordered phase cannot be reformed from the **TPA-C_{60}** melt. Oriented crystal arrays of **TPA-C_{60}**, which contain flat-on TPA/C_{60} nano-stacks can be obtained via the PDMS-assisted crystallization (PAC) technique. The flat-on dual-channel supramolecular structure of **TPA-C_{60}** delivered ambipolar and balanced charge-transport characteristics with averaged μ_e of 2.11×10^{-4} $cm^2V^{-1}s^{-1}$ and μ_h of 3.37×10^{-4} $cm^2V^{-1}s^{-1}$. The anisotropic charge-transport ability of the pyramid-sphere shape amphiphile was further understood based on the lattice structure and the lattice orientation of **TPA-C_{60}** revealed from the electron diffraction analyses.

1.Introduction

Giant shape amphiphiles are synthesized by covalently binding various nm-sized molecular building blocks (or the so-called molecular nanoparticles (MNPs)).[1] Their self-assembly processes are driven by the competitive or cooperative physical interactions among the MNPs, and are largely influenced by the preferred packing scheme of the constituent MNPs. The giant shape amphiphiles contain a wide range of emerging materials,[1, 2] such as the sphere-cube,[1] sphere-board,[3-5], sphere-disc,[6-19] discotic−rod,[20,21] cube-disk,[22] and cube-board[23] shape amphiphiles. Among these giant molecules, those built with *p*-type and *n*-type conjugated moieties attracted much attention, because of their potential applications as the active units in the supramolecular optoelectronics.[5, 24, 25]

Giant molecules can be constructed from crystalline mesogenic, quasicrystalline and amorphous MNPs, [26] but so far, most giant shape amphiphiles are made with MNPs that are intrinsically crystalline. Triphenylamine (TPA) based conjugated molecules are widely used in organic light emitting diodes (OLEDs),[27,28] polymer solar cells (PSCs),[29] and pervoskite solar cells,[30] because of their good morphological stability and *p*-type semiconducting characteristics. However, they are rarely reported as a MNP of giant shape amphiphiles, probably due to their nonplanar structure and amorphous nature.[27, 28] The incorporation of this pyramidal nano-building block raises interesting questions, such as will the self-organization of a giant shape amphiphile be compromised due to the presence of the amorphous nano-pyramid, or on the opposite, will the amorphous nano-pyramid self-organizes because the other MNP of the giant shape amphiphile tends to crystallize? To look into the question, a giant pyramid-sphere shape amphiphile, **TPA-C_{60}**, which is constructed with the amorphous nano-pyramid (TPA) and the crystalline nano-sphere (C_{60}), was designed and synthesized based on Steglich esterification and copper-catalyzed azide-alkyne cycloaddition (CuAAC), as shown in Scheme 1. The phase behavior and phase structure of **TPA-C_{60}** were investigated via differential scanning calorimetry (DSC), and electron diffraction (ED). The field effect transistor (FET) characteristics of **TPA-C_{60}** were evaluated with the oriented **TPA-C_{60}** crystal arrays prepared via the PDMS-assisted crystallization (PAC) method.[31] The results show that the pyramid-sphere shape amphiphile self-organized into an ordered phase containing stacks of alternating two-dimensional (2D) C_{60} and TPA nanosheets. Moreover, this dual-channel supramolecular structure of TPA-C_{60} delivered ambipolar and balanced charge-transport characteristics in the organic field-effect transistors (OFETs). Previous studies showed that TPA and C_{60} have preferable physical interaction and tend to form mixed TPA/C_{60} domain in the solid-state. [32-34] However, in the aspect of functions, the mixed TPA/C_{60} domain is not conducive for the ambipolar charge transport. Our study thus gives the first example of the flat-on ambipolar TPA/C_{60} nano-stacks obtained via the self-organization of a pyramid-sphere shape amphiphile.

[a] *Department of Applied Chemistry, National Chiao Tung University, 1001 Ta Hsueh Road Hsin-Chu, 30010, Taiwan Address here.*
**E-Mail: kclwang@nctu.edu.tw*
‡ Wei-Wei Liang and Chi-Feng Huang are joint first authors.
† Electronic Supplementary Information (ESI) available: 1H and 13C NMR spectra, TGA, DSC, XRD, Simulated ED patterns, UV-Vis spectra, reduction and oxidation cyclic voltammetry curves. CCDC 1415320–1415323. See DOI: 10.1039/x0xx00000x

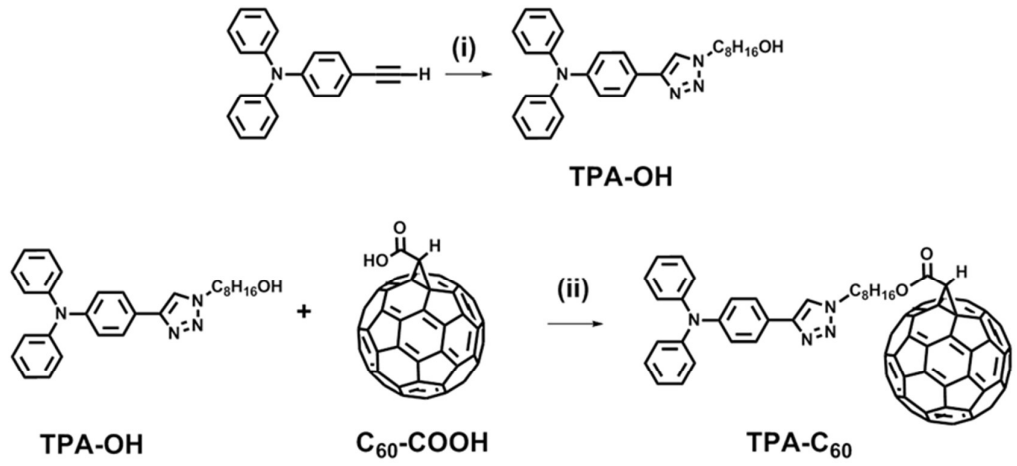

Scheme 1. Synthetic route of **TPA-C_{60}**. Reagents and conditions: (i) 8-azidooctan-1-ol, copper(II) sulfate pentahydrate, sodium ascorbate, THF/H_2O (1/1, v/v); (ii) *p*-toluenesulfonic acid, 4-dimethylaminopyridine, 1-(3-dimethylaminopropyl)-2-ethylcarbodiimide hydrochloride, CS_2

2. Results and discussion

2.1. Synthesis of TPA-C_{60}

Scheme 1 shows the synthetic route of **TPA-C_{60}**. 4-ethynyl-N,N-diphenylaniline, 8-azidooctan-1-ol, and fullerenoacetic acid (C_{60}-COOH) were synthesized according to the literature.[35] Reacting 4-ethynyl-N,N-diphenylaniline with 8-azidooctan-1-ol via the CuAAC allowed the formation of the *p*-type pyramid unit, 8-(4-(triphenylamino)-1H-1,2,3-triazol-1-yl)octan-1-ol (TPA-OH) in 67% yield. The final product, **TPA-C_{60}**, was then synthesized in 74% yield by reacting TPA-OH and C_{60}-COOH via Steglich esterification. **TPA-C_{60}** was characterized by ^{1}H NMR, ^{13}C NMR, and mass spectrometry. In Fig. S1, the formation of the **TPA-C_{60}** was identified by the downfield shift of the methylene protons of TPA-OH (denoted as H_a in Fig. S1) and the appearance methine proton (H_b in Fig. S1b) at δ = 4.88 ppm, which belongs to the C_{60} moiety. The multiple peaks between δ = 135~145 ppm in the ^{13}C-NMR spectrum of **TPA-C_{60}** (Fig. S2b), are also the characteristic of the sp^2 carbons on the mono-adduct C_{60} moiety. Furthermore, in Fig. S3, the $[M+H]^+$ peak of the final product has the *m/z* value of 1201.267, which matches well with the calculated monoisotopic mass (1201.24 Da). All the results clearly indicate the success of the reaction and confirm the chemical identity and purity of **TPA-C_{60}**.

2.2. Thermal stability and phase transition

After vacuum dried by a cryo pump, the thermogravimetry analysis in Fig. S4a shows a 5% weight loss temperature of **TPA-C_{60}** is at 388 °C. As shown in Fig. S4b, an additional weight loss peak at 131 °C was observed for the **TPA-C_{60}** sample vacuum dried only under a mechanical pump. The results indicate that the as-precipitate **TPA-C_{60}** contains residue solvent molecules that can be removed under high vacuum. DSC was then applied to identify the phase behaviours of the two MNPs and the pyramid-sphere shape amphiphile. In Fig.S5a, 4-ethynyl-N,N-diphenylaniline show an endothermic first-order transition at 108 °C during the 1st heating, suggesting the as-precipitated sample self-organized into an ordered phase. However, the corresponding exothermic transition in the subsequent cooing was not observed, indicating that 4-ethynyl-N,N-diphenylaniline was vitrified rather than crystallized in the cooling process. Consequently, in the 2nd heating (Fig. S5b), the endothermic transition at 108 °C disappeared. In Fig. S5c,**TPA-OH** exhibits only glass transition temperature at 10 °C. Thus, the results show the easily disturbed self-organization behaviour of the TPA unit; i.e. although 4-ethynyl-N,N-diphenylaniline self-organizes from the solution, the behaviour is lost in the melt, and when a flexible alkyl group is attached. For **TPA-C_{60}**, three first-order transitions at 190, 226 and 239 °C were found in the 1st heating curve of **TPA-C_{60}** (Fig. S5d), indicating that **TPA-C_{60}** packs into ordered solid-state structure. The multiple transitions suggest that instead of directly transforming into the isotropic melt, the ordered phase of **TPA-C_{60}** may lose its structural order (conformational, orientational, and positional orders) in a stepwise way. In the cooling curve, no exothermic peak was observed, indicating that although self-organization of **TPA-C_{60}** from solution is possible, reforming the ordered packing from the melt is difficult, probably due to the structural complexity of **TPA-C_{60}**. In short, the DSC results revealed the amorphous nature of the alkylated TPA nano-pyramid, and the crystalline characteristic of the **TPA-C_{60}** shape amiphiphile. More importantly, it was found that the amorphous alkylated nano-pyramid (TPA) can self-assemble under the assistance of the favourable intermolecular interactions among the crystalline nano-spheres (C_{60}).

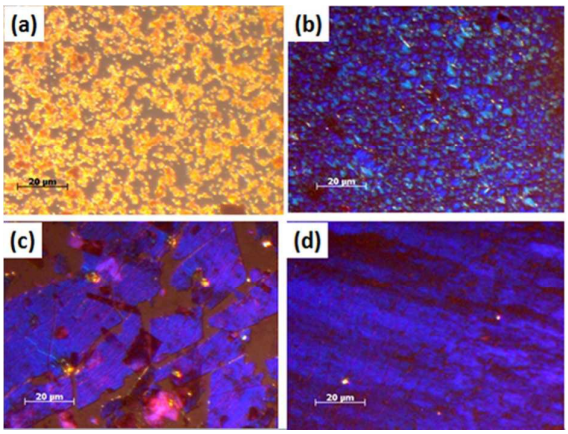

Fig. 1 POM images of **TPA-C_{60}** processed via the PAC method with different solvents. (a) m-xylene, (b) CS_2, (c) ODCB, and (d) TCB

2.3 Phase morphology of TPA-C_{60}

TPA-C_{60} tends to form tiny crystals in drop-casted thin films. To obtain crystals large enough for device fabrication, and to introduce better crystal orientation, the PAC method [31] was applied to produce the crystal array of **TPA-C_{60}**. Fig. 1 shows the **TPA-C_{60}** films obtained from different solvents. In Fig. 1a and 1b, the crystal sizes are small when **TPA-C_{60}** was processed from the m-xylene and CS_2 solutions. However, the bright blue or yellow POM images suggested that **TPA-C_{60}** has birefringence and structural order in the casted films. Large crystalline **TPA-C_{60}** sheets were obtained from the *o*-dichlorobenzene (ODCB) and 1,2,4-trichlorobenzene (TCB) solutions (Fig. 1c and 1d). Intriguingly, as shown in Fig. S6, the color of the crystalline sheet was only observed when the incident light is polarized (Fig. S6c and S6d), and the crystal does not turn dark even when its growth direction is along the polarization direction of the polarizer or the analyzer. Similar phenomenon was observed in the blue phases of highly chiral liquid crystals.[36] The origin of the blue or yellow POM images of **TPA-C_{60}** falls outside the scope of the current work, and will be investigated separately.

The AFM topography and cross-section profile in Fig. 2 show that the **TPA-C_{60}** film prepared from the ODCB solution is a polycrystalline thin film with very rough surface (max thickness ~ 80 nm), but the one prepared from the TCB solution has insignificant crystalline boundary and uniform surface (thickness ~ 150 nm). The crystal array prepared from TCB was further examined with transmission electron microscopy (TEM) and electron diffraction (ED). Similar to the AFM result, the **TPA-C_{60}** crystal has uniform appearance in the TEM image (Fig. 3a). The clear diffraction spots in the ED pattern (Fig. 3b) give the evidence of the formation of ordered solid-state structure, and more importantly, the well-oriented crystal lattices in the **TPA-C_{60}** crystal array by the PAC method. These morphological characterizations thus confirmed that the pyramid-sphere shape amphiphile, **TPA-C_{60}**, can assemble into an ordered phase, and a good lattice orientation can be induced via the PAC method.

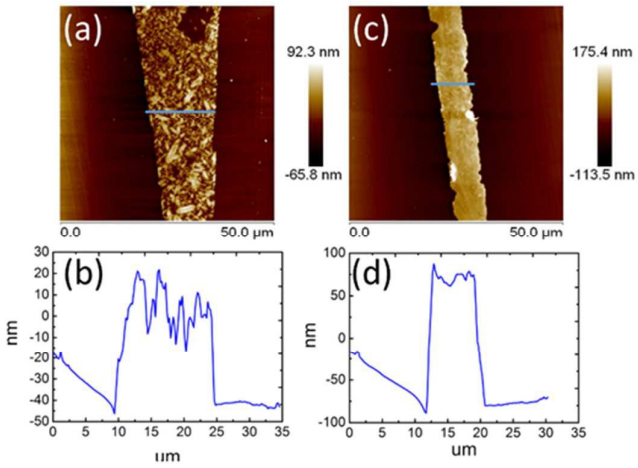

Fig. 2 AFM topography and cross-section profiles of **TPA-C_{60}** processed via the PAC method with ODCB (a), (b) and TCB (c), (d).

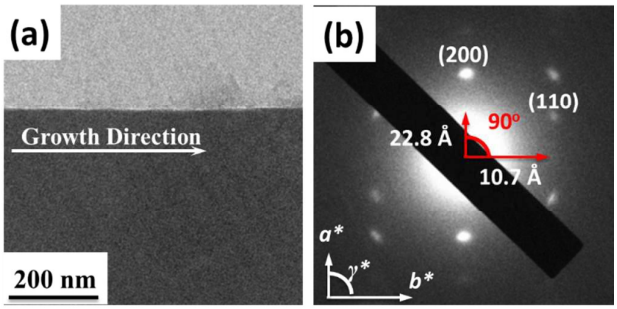

Fig. 3 (a) TEM image and (b) the enlarged ED pattern of the **TPA-C_{60}** crystal array prepared via the PAC method using TCB as solvent.

2.4. Phase structure of TPA-C_{60}

Due to the structural complexity, preparation of large-sized single crystal of **TPA-C_{60}** for single-crystal structural characterization was difficult. Nevertheless, the ED patterns along different zone axes are still useful to reveal the 2D lattice projections of the **TPA-C_{60}** crystal. By using the drop-casting sample, the *a*b** and the *b*c** reciprocal lattices (Fig. 4b and 4c) were observed. The lattice parameters deduced from Fig. 4b are a = 22.8 Å, b =10.7 Å, γ = 90°; and from Fig. 4c are b = 10.7 Å, c = 51.0 Å, and α = 90°. The measured density of the **TPA-C_{60}** crystal is 1.28 g cm^{-1}. Assumed that β = 90°, the density provides the information that the orthorhombic lattice (a = 22.8 Å, b =10.7 Å, c =51.0 Å, α = β = γ = 90°) contains 8 **TPA-C_{60}** molecules per unit cell. The powder X-ray diffraction (XRD) pattern of **TPA-C_{60}** is shown in Fig. S7. The theoretical d-spacings of various lattice planes calculated from the above lattice parameters also match the measured ones (Table S1). Furthermore, the (100) and (010) diffractions in Fig. 4b are significantly weaker than the (200) and (020) diffractions, suggesting that in the lattice, the electron density on the (100) planes is close to that on the (200) planes, and that on the (010) planes is also similar to that on the (020) planes. The lattice model was then built in the Cerius[2] software package based on the above information, and shown in Fig. 5. The simulated ED patterns (Fig. S8) generated from the [001] and

Table 1. OFET characteristics of the TPA-C60 crystal arrays

	$\mu_{e\ average}$ ($cm^2 V^{-1} s^{-1}$)	I_{on} / I_{off}	V_{th} (V)	$\mu_{h\ average}$ ($cm^2 V^{-1} s^{-1}$)	I_{on} / I_{off}	V_{th} (V)
Parallel	2.11×10^{-4}	3×10^{4}	32	3.37×10^{-4}	6×10^{3}	−22
Perpendicular	3.54×10^{-5}	1×10^{1}	16	5.43×10^{-5}	2×10^{3}	−15

*The μs of the parallel devices were averaged from 8 devices, and those of the perpendicular device were averaged from 6 devices.

[100] zones of the model resemble the experimental ones in Fig. 5, showing the validity of the model. The lattice of **TPA-C_{60}** features the dual-channel structure containing the continuous, but separated 2D *n*-type C_{60} sheets and *p*-type TPA sheets (Fig. 5b). Noteworthy, the C_{60}-to-C_{60} distance along the *a* axis (11.4 Å) is different from that along and *b* axis (10.7 Å). The ED of the crystal array prepared by PAC (Fig. 4a) shares the same zone axis, [001], with the pattern in Fig. 4b. Thus, it is confirmed that in the PAC method, the growth direction of the crystal array is along the *b* axis the **TPA-C_{60}** lattice, and the 2D C_{60} and TPA sheets adopt a flat-on orientation of the substrate.

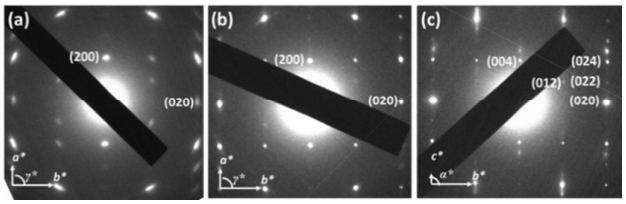

Fig. 4 The ED patterns of **TPA-C_{60}** crystal prepared from (a) the PAC method. (b) and (c) from drop-casting. The projections of the *a*b** and the *b*c** reciprocal lattices can be seen in (b) and (c).

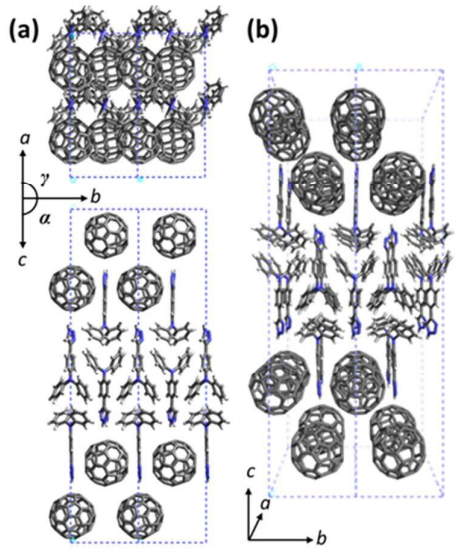

Fig. 5 The lattice model of **TPA-C_{60}**. (a) The *ab* and the *bc* lattice projections, and (b) the projection view of the lattice.

2.5. Optical and electrochemical properties

The UV-Vis absorption spectrum and cyclic voltammogram (CV) of **TPA-C_{60}** are shown in Fig. S9 and S10. For comparison, the absorption spectra and the CVs of [6,6]-phenyl-C61-butyric acid methyl ester (PCBM) and TPA-OH are also included in the figures. As shown in Fig. S6, the absorption maximum of **TPA-C_{60}** is similar to that of PCBM. The slightly stronger absorption at 315 nm was attributed to the TPA moiety of **TPA-C_{60}**. In Fig. S10, there shows three reversible reductions and one oxidation. The reduction potential, oxidized potential, HOMO and LUMO energy of the three compounds are summarized in Table S2. The HOMO and LUMO energies of **TPA-C_{60}** are close to the HOMO energy of TPA-OH and the LUMO energy of PCBM, suggesting that the C_{60} and TPA moieties of **TPA-C_{60}** retain their individual characteristics in the molecule.

2.6. OFET performance

The charge transport properties of the oriented **TPA-C_{60}** crystal arrays prepared by the PAC method were investigated in OFET devices with a bottom-gate, top-contact configuration. Since the ED result confirmed that the *b* lattice axis of **TPA-C_{60}** is parallel to the crystal growth direction induced by PAC, as shown in Fig. 6, the source and drain electrodes were arranged parallel, or perpendicular to the growth direction, so that the anisotropic charge-transport characteristics of the **TPA-C_{60}** crystal arrays along the *a* and *b* axes can be studied. The output and transfer plots of the best-performed device are shown in Fig. 7. The **TPA-C_{60}** crystal array demonstrated the *p*-channel characteristics under the negative gate-to-source voltage (V_{GS}) (Fig. 7a), and the *n*-channel characteristics under the positive V_{GS} (Fig. 7b). The hole mobilities (μ_hs) and electron mobilities (μ_es) deduced from the transfer plots of the devices in saturation regimes are summarized in Table 1. The averaged μ_hs are 3.37×10^{-4} $cm^2 V^{-1} s^{-1}$ for the parallel devices and 5.43×10^{-5} $cm^2 V^{-1} s^{-1}$ for the perpendicular devices. In the database we have searched, the highest OFET μ_h of TPA-star burst conjugated molecules was around 3×10^{-4} $cm^2 V^{-1} s^{-1}$.[37] Thus, the 2D sheets of TPA in the **TPA-C_{60}** crystal array retain their hole-transporting ability, and delivered one of the best μ_h among the triarylamine based molecules. On the other hand, the 2D sheets of the mono-adduct C_{60} delivered the averaged μ_es of 2.11×10^{-4} $cm^2 V^{-1} s^{-1}$ for the parallel devices, and 3.54×10^{-5} $cm^2 V^{-1} s^{-1}$ for the perpendicular devices. Thus, the **TPA-C_{60}** crystal array has ambipolar charge transport characteristic, and delivered balanced hole and electron

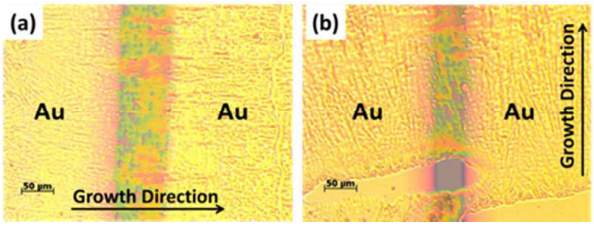

Fig. 6 The OM images of the **TPA-C_{60}** OFET devices with the Gold (Au) source and drain electrodes arranged (a) parallel, and (b) perpendicular to the crystal growth direction.

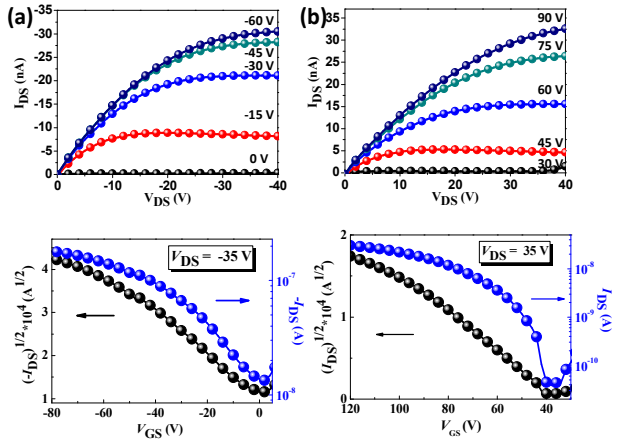

Fig. 7 The output (up) and transfer (down) characteristics of the **TPA-C_{60}** crystal arrays under (a) negative V_{GS}, and (b) positive V_{GS}.

charge mobilities. Moreover, the anisotropic charge-transport characteristic of the **TPA-C_{60}** crystal array is obvious, because the μ_h and μ_e along the growth direction (*b* lattice axis) is about one order of magnitude higher than those perpendicular to the growth axis (*a* lattice axis). The difference can be attributed to the shorter TPA-TPA and C_{60}-C_{60} distances along the *b* axis, as shown in the *ab* lattice projection of Fig. 5a. The lower μ_e of the **TPA-C_{60}** crystal array compared to the best-performed C_{60} OFETs may be related to the longer C_{60}-C_{60} distance and the lower coordination number of the C_{60}s in the **TPA-C_{60}** crystal lattice.[31, 38] In addition, the smeared ED pattern in Fig. 4a also suggests certain degree of orientational disorder in the crystal array, which is also detrimental to the μ_e.

3.Conclusions

In summary, the synthetic route of a giant shape amphiphile (**TPA-C_{60}**), which is constructed with an amorphous pyramid (TPA) and a crystalline sphere (C_{60}), was developed. DSC results show that the pyramid-sphere shape amphiphile forms a solvent-induced ordered phase, because of the strong crystalline nature of the C_{60} moiety. Structural characterizations confirmed that **TPA-C_{60}**s self-assemble into separated 2D C_{60} and TPA sheets in the ordered phase. Processed with the PAC method, oriented crystal arrays of **TPA-C_{60}** can be prepared. ED results indicate that the 2D C_{60} and TPA sheets adopt a flat-on orientation on the substrate with its *b* lattice axis points to the crystal growth direction. The flat-on *n*-type C_{60} nano-sheets and *p*-type TPA nano-sheets provide electron and hole transporting channels. Ambipolar and balanced charge-transport characteristics were delivered by the **TPA-C_{60}** crystal arrays in OFET devices. The dual-channel supramolecular structure of **TPA-C_{60}** delivered averaged μ_e of 2.11×10^{-4} $cm^2V^{-1}s^{-1}$ and μ_h of 3.37×10^{-4} $cm^2V^{-1}s^{-1}$. The μ_h is comparable to the best-performed triaryl amine based *p*-type conjugated molecules, while modest μ_e delivered by the C_{60} nano-sheets was attributed to the longer C_{60}-C_{60} distance, the lower C_{60} coordination number in the **TPA-C_{60}** crystal lattice, and the less orientational order of the **TPA-C_{60}** crystal array, comparing to the pristine C_{60} crystals. Although the 2D crystal array of C_{60} has been recently disclosed,[39] our study revealed the first example of dual-channel self-organized structure and the ambipolar characteristic of a novel giant pyramid-sphere shape amphiphile.

4. Experimental section

General Measurement and Characterization. UV-Vis experiment was carried out by the HITACHI U-4100 spectrophotometer to a 10^{-3} M solution concentration in o-dichlorobenzene. The cyclic voltammetry (CV) data were analyzed by a CH Instruments Model 611D with a carbon glass served as the working electrode and Ag/Ag+ electrode as the reference electrode, while 0.1 M tetrabutylammonium hexafluorophosphate (Bu_4NPF_6) as the electrolyte and 10^{-2} M desired compound dissolved in o-dichlorobenzene. Thermogravimetric analysis (TGA) was based on a Perkin-Elmer Pyris under inert atmosphere with a heating rate of 10 °C/min and differential scanning calorimeter (DSC) was measured on TA Q200 Instrument at a temperature ramp rate of 5 °C/min. For 1D XRD patterns, Bruker APEX DUO single crystal diffraction and an APEX II CCD camera equipped with a INCOATEC 18 kW rotating I microfocus X-ray generator (Cu Kα radiation (0.1542 nm)) were used. Transmission Electron Microscopy (TEM) observations were performed on a JEOL JEM-2010 transmission electron microscope with an accelerating voltage of 160 kV and a Gatan-831 CCD camera. Crystal simulation and drawing were based on Cerius^2 software product from Accelrys.

OFET Fabrication. A *n*-type heavily doped Si wafer with a SiO_2 layer of 300 nm and a capacitance of 11.5 nF/cm^2 as the gate electrode and dielectric layer was ultrasonically cleaned sequentially in detergent, water and isopropyl alcohol. n-octadecyltrichlorosilane (ODTS) was used as the self-assembled monolayer. The **TPA-C_{60}** crystal arrays were prepared via the PDMS assisted crystallization (PAC) method.[31] The gold source and drain electrodes (40 nm in thickness) were then deposited on the organic layer by vacuum evaporation through a shadow mask, affording a bottom-gate-top-contact device configuration. OFET measurement was carried out at room temperature under nitrogen atmosphere using Agilent Technologies 4156C instrument. The mobility calculation was based on the equation $I_{ds} = (W/2L)\mu C_i(V_g - V_t)^2$ in saturation regime, where I_{ds} is the drain-source current, W is the channel width (1 mm), L is the channel length (100 μm), μ is the field-effect mobility, C_i is the capacitance per unit area of

the dielectric layer, V_g is the gate voltage, and V_t is threshold voltage.

Synthesis. All chemicals are purchased from Aldrich, Acros or TCI and used as received unless specified in synthetic scheme. ^{1}H and ^{13}C NMR spectra were measured in deuterium substituted chloroform $CDCl_3$ as the reference with 0.5 wt % TMS using Varian 400 MHz instrument spectrometers.

8-(4-(triphenylamino)-1H-1,2,3-triazol-1-yl)octan-1-ol (TPA-OH). To a solution of 4-ethynyl-N,N-diphenylaniline **3** (0.5 g, 1.86 mmol), copper(II) sulfate pentahydrate (0.046 g, 0.184 mmol) and Sodium ascorbate (0.11 g, 0.56 mmol) was added 8-azidooctan-1-ol **5** (0.382 g, 2.23 mmol) in THF/H_2O 50 ml (1/1, v/v). The reaction mixture was stirred at room temperature for 3 hours then extracted by dichloromethane and water. The organic layer was collected and dried by $MgSO_4$. After removal of the solvent under reduced pressure, the residue was purified by silica gel chromatography with ethyl acetate/hexane (1/3, v/v) as the eluent to give a beige solid (0.55 g, 67%). ^{1}H NMR (400 MHz, $CDCl_3$): δ 1.31–1.34 (m, 8H), 1.54 (t, 2H, J = 7 Hz), 1.93 (t, 2H, J = 7 Hz), 3.62 (t, 2H, J = 6.6 Hz), 4.37 (t, 2H, J = 7.2 Hz), 7.02 (t, 2H, J = 7.2 Hz), 7.12 (d, 6H), 7.24 (d, 2H), 7.26 (d, 2H), 7.66 (d, 2H), 7.69 (s, 1H). ^{13}C NMR ($CDCl_3$, 100 MHz): δ 25.6, 26.4, 28.9, 29.1, 30.3, 32.6, 50.3, 62.9, 118.8, 123.0, 123.8, 124.5, 124.7, 126.6, 129.3, 147.5, 147.7. MS (EI, $C_{28}H_{32}N_4O$): calcd, 440.58; found, 440.5.

8-(4-(triphenylamino)-1H-1,2,3-triazol-1-yl)octyl acetate C_{60} (TPA-C_{60}). To a solution of C_{60}-COOH (70 mg, 0.09 mmol), *p*-toluenesulfonic acid (17 mg, 0.09 mmol), 4-dimethylaminopyridine (11 mg, 0.09 mmol) and 1-(3- dimethylaminopropyl)-2-ethylcarbodiimide hydrochloride (17 mg 0.09 mmol) was added 8-(4-(triphenylamino)-1H-1,2,3-triazol-1-yl)octan-1-ol (60 mg, 13.6 mmol) in carbon disulfide (20 ml), the reaction mixture was stirred at room temperature for 12 hours. After removal of the solvent under reduced pressure, the residue was purified by neutral aluminum oxide chromatography with toluene to give a brown solid (79 mg, 74%). ^{1}H NMR (400 MHz, $CDCl_3$): δ 1.30–1.59 (m, 8H), 1.85 (t, 2H, J = 7.4 Hz), 1.95 (t, 2H, J = 7.4 Hz), 4.38 (t, 2H, J = 7.2 Hz), 4.45 (t, 2H, J = 6.6 Hz), 4.78 (s, 1H), 7.02 (t, 2H, J = 7.2 Hz), 7.10 (d, 6H), 7.24 (d, 2H), 7.26 (d, 2H), 7.67 (d, 2H), 7.69 (s, 1H). ^{13}C NMR ($CDCl_3$, 100 MHz): δ 25.9, 26.4, 28.6, 30.0, 30.4, 39.1, 50.3, 66.4, 70.6, 77.2, 118.8, 123.0, 123.8, 124.5, 124.8, 126.6, 129.3, 136.4, 140.4, 140.9, 141.1, 142.0, 142.1, 142.2, 142.4, 142.8, 143.0, 143.1, 143.2, 143.7, 143.9, 144.4, 144.6, 144.7, 145.0, 145.1, 145.2, 145.3, 145.6, 145.8, 147.5, 147.6, 147.7, 148.3, 166.4; MS ($C_{90}H_{32}N_4O_2$): calcd, 1201.24; found(FAB), 1200.9; found (MALDI-TOF), 1201.267.

Acknowledgements

This work is supported by the Ministry of Science and Technology, Taiwan (MOST 103-2221-E-009-213-MY3, MOST 104-2628-E-009-007-MY3) and "ATP" of the National Chiao Tung University and Ministry of Education, Taiwan.

Notes and references

1. W.-B. Zhang, X. Yu, C.-L. Wang, H.-J. Sun, I. F. Hsieh, Y. Li, X.-H. Dong, K. Yue, R. Van Horn and S. Z. D. Cheng, *Macromolecules*, 2014, **47**, 1221-1239.
2. S. C. Glotzer, *Science*, 2004, **306**, 419-420.
3. F. A. Teng, Y. Cao, Y. J. Qi, M. Huang, Z. W. Han, S. Z. Cheng, W. B. Zhang and H. Li, *Chem. Asian J.*, 2013, **8**, 1223-1231.
4. J. Baffreau, L. Ordronneau, S. Leroy-Lhez and P. Hudhomme, *J. Org. Chem.*, 2008, **73**, 6142-6147.
5. W.-S. Li, Y. Yamamoto, T. Fukushima, A. Saeki, S. Seki, S. Tagawa, H. Masunaga, S. Sasaki, M. Takata and T. Aida, *J. Am. Chem. Soc.*, 2008, **130**, 8886-8887.
6. C.-L. Wang, W.-B. Zhang, H.-J. Sun, R. M. Van Horn, R. R. Kulkarni, C.-C. Tsai, C.-S. Hsu, B. Lotz, X. Gong and S. Z. D. Cheng, *Adv. Energy Mater.*, 2012, **2**, 1375-1382.
7. C.-L. Wang, W.-B. Zhang, X. Yu, K. Yue, H.-J. Sun, C.-H. Hsu, C.-S. Hsu, J. Joseph, D. A. Modarelli and S. Z. D. Cheng, *Chem. Asian J.*, 2013, **8**, 947-955.
8. S. V. Kirner, D. M. Guldi, J. D. Megiatto, Jr. and D. I. Schuster, *Nanoscale*, 2015, **7**, 1145-1160.
9. D. I. Schuster, P. D. Jarowski, A. N. Kirschner and S. R. Wilson, *J. Mater. Chem.*, 2002, **12**, 2041-2047.
10. H. Imahori, *Org. Biomol. Chem.*, 2004, **2**, 1425-1433.
11. R. Chitta and F. D'Souza, *J. Mater. Chem.*, 2008, **18**, 1440-1471.
12. S. V. Kirner, D. Arteaga, C. Henkel, J. T. Margraf, N. Alegret, K. Ohkubo, B. Insuasty, A. Ortiz, N. Martín and L. Echegoyen, *Chem. Sci.*, 2015, **6**, 5994-6007.
13. H. Hayashi, W. Nihashi, T. Umeyama, Y. Matano, S. Seki, Y. Shimizu and H. Imahori, *J. Am. Chem. Soc.*, 2011, **133**, 10736-10739.
14. H. Imahori, T. Umeyama, K. Kurotobi and Y. Takano, *Chem. Commun.*, 2012, **48**, 4032-4045.
15. F. Wessendorf, B. Grimm, D. M. Guldi and A. Hirsch, *J. Am. Chem. Soc.*, 2010, **132**, 10786-10795.
16. G. Liu, A. N. Khlobystov, G. Charalambidis, A. G. Coutsolelos, G. A. Briggs and K. Porfyrakis, *J. Am. Chem. Soc.*, 2012, **134**, 1938-1941.
17. D. I. Schuster, K. Li, D. M. Guldi, A. Palkar, L. Echegoyen, C. Stanisky, R. J. Cross, M. Niemi, N. V. Tkachenko and H. Lemmetyinen, *J. Am. Chem. Soc.*, 2007, **129**, 15973-15982.
18. P. A. Liddell, G. Kodis, A. L. Moore, T. A. Moore and D. Gust, *J. Am. Chem. Soc.*, 2002, **124**, 7668-7669.
19. M. Wolffs, F. J. Hoeben, E. H. Beckers, A. P. Schenning and E. Meijer, *J. Am. Chem. Soc.*, 2005, **127**, 13484-13485.
20. R. W. Date and D. W. Bruce, *J. Am. Chem. Soc.*, 2003, **125**, 9012-9013.
21. G. Bottari, G. de la Torre, D. M. Guldi and T. S. Torres, *Chem. Rev.*, 2010, **110**, 6768-6816.
22. L. Cui, J. P. Collet, G. Xu and L. Zhu, *Chem. Mater.*, 2006, **18**, 3503-3512.
23. H. Araki and K. Naka, *J. Polym. Sci. A Polym. Chem.*, 2012, **50**, 4170-4181.
24. R. Charvet, Y. Yamamoto, T. Sasaki, J. Kim, K. Kato, M. Takata, A. Saeki, S. Seki and T. Aida, *J. Am. Chem. Soc.*, 2012, **134**, 2524-2527.
25. H. Imahori, D. M. Guldi, K. Tamaki, Y. Yoshida, C. Luo, Y. Sakata and S. Fukuzumi, *J. Am. Chem. Soc.*, 2001, **123**, 6617-6628.
26. P. F. Damasceno, M. Engel and S. C. Glotzer, *Science* 2012, **337**, 453-457.
27. D. F. O'Brien, P. E. Burrows, S. R. Forrest, B. E. Koene, D. E. Loy and M. E. Thompson, *Adv. Mater.*, 1998, **10**, 1108-1112.
28. P. Strohriegl and J. V. Grazulevicius, *Adv. Mater.*, 2002, **14**, 1439-1452.

29. C.-Y. Chang, L. Zuo, H.-L. Yip, Y. Li, C.-Z. Li, C.-S. Hsu, Y.-J. Cheng, H. Chen and A. K. Y. Jen, *Adv. Funct. Mater.*, 2013, **23**, 5084-5090.
30. M. M. Lee, J. Teuscher, T. Miyasaka, T. N. Murakami and H. J. Snaith, *Science*, 2012, **338**, 643-647.
31. K.-Y. Wu, T.-Y. Wu, S.-T. Chang, C.-S. Hsu and C.-L. Wang, *Adv. Mater.*, 2015, **27**, 4371-4376.
32. L. Y. Chiang, P. A. Padmawar, T. Canteenwala, L.-S. Tan, G. S. He, R. Kannan, R. Vaia, T.-C. Lin, Q. Zheng and P. N. Prasad, *Chem. Commun.*, 2002, 1854-1855.
33. D. Konarev, A. Y. Kovalevsky, A. Litvinov, N. Drichko, B. Tarasov, P. Coppens and R. Lyubovskaya, *J. Solid State Chem.*, 2002, **168**, 474-485.
34. S. Clavaguera, S. I. Khan and Y. Rubin, *Org. Lett.*, 2009, **11**, 1389-1391.
35. B. Ma, C. E. Bunker, R. Guduru, X.-F. Zhang and Y.-P. Sun, *J. Phys. Chem. A*, 1997, **101**, 5626-5632.
36. H.-S. Kitzerow and C. Bahr, *Chirality in Liquid Crystals*, Springer-Verlag, New York, 2001, ch. 7, pp. 186.
37. M. Sonntag, K. Kreger, D. Hanft, P. Strohriegl, S. Setayesh and D. de Leeuw, *Chem. Mater.*, 2005, **17**, 3031-3039.
38. H. Li, B. C. Tee, J. J. Cha, Y. Cui, J. W. Chung, S. Y. Lee and Z. Bao, *J. Am. Chem. Soc.*, 2012, **134**, 2760-2765.
39. X. Zhang, C. H. Hsu, X. Ren, Y. Gu, B. Song, H. J. Sun, S. Yang, E. Chen, Y. Tu, X. Li, X. Yang, Y. Li and X. Zhu, *Angew. Chem. Int. Ed.*, 2015, **54**, 114-117.